Topographically Trapped Waves Around South America With Periods Between 40 and 130 Days in a Global Ocean Reanalysis

Léa Poli, Camila Artana, Christine Provost

JGR Oceans

RESEARCH ARTICLE
10.1029/2021JC018067

Key Points:

- Coherent Sea Level Anomalies indicate trapped waves propagation along the slope from the Equatorial Pacific to the Tropical Atlantic (22°S)
- The Madden-Julian Oscillation (MJO), through oceanic and atmospheric teleconnections, plays a key role in forcing the trapped waves
- Furthermore, local winds trigger waves in specific locations, such as the south-east Pacific and the Brazil-Malvinas Confluence

Correspondence to:
L. Poli,
lea.poli@locean.ipsl.fr

Citation:
Poli, L., Artana, C., & Provost, C. (2022). Topographically trapped waves around South America with periods between 40 and 130 days in a global ocean reanalysis. *Journal of Geophysical Research: Oceans*, *127*, e2021JC018067. https://doi.org/10.1029/2021JC018067

Received 29 SEP 2021
Accepted 2 FEB 2022

Topographically Trapped Waves Around South America With Periods Between 40 and 130 Days in a Global Ocean Reanalysis

Léa Poli[1], Camila Artana[2], and Christine Provost[1]

[1]Laboratoire LOCEAN-IPSL, Sorbonne Université (UPMC, Univ. Paris 6), CNRS, IRD, MNHN, Paris, France, [2]Mercator Ocean, Toulouse, France

Abstract The South American continental slope hosts a variety of topographic waves. We use a 27-year-long global ocean reanalysis (1/12° Spatial resolution) to examine trapped waves (TWs) around South America at periods ranging from 40 to 130 days. The waves propagate from the Equatorial Pacific to the Tropical Atlantic (22°S) with phase velocities between 1.8 and 7 m/s according to the local background characteristics, such as stratification, slope steepness, latitude, mean flow and shelf width. The Madden-Julian Oscillation (MJO) plays a key role in forcing the TWs in two ways (a) through an oceanic connection implying equatorial Kelvin waves reaching the western American Coast and (b) through an atmospheric teleconnection enhancing southerly winds in the south-east Pacific. Furthermore, local winds, not necessarily linked with the MJO, modulate and trigger waves in specific locations, such as the Brazil-Malvinas Confluence. Trapped waves impact the along-shore currents: during the positive phase of the waves the near-surface flow is enhanced by about 0.1 m/s.

Plain Language Summary Several waves propagate around South America from the Equatorial Pacific to the Tropical Atlantic (22°S) along the continental slope. The waves propagate relatively fast with velocities varying between 1.8 and 7 m/s depending on the local background for example, the continental slope geometry. Two forcing mechanisms were identified: a Pacific Equatorial forcing associated with climatic indices and a local wind forcing at specific locations such as the south-east Pacific and the Brazil-Malvinas Confluence. The waves impact the along-shore currents: the flow is modulated by about 0.1 m/s.

1. Introduction

The South American continental slope hosts a variety of sub-inertial trapped waves (TWs) propagating with the coast to their left with periods ranging from few days to months (Clarke, 1992; Brink, 1982, Figure 1a). TWs have been documented both on the Pacific and Atlantic continental slope from in-situ data and model studies.

The Pacific Ocean equatorial dynamics, mainly modulated by the El Niño Southern Oscillation (ENSO) and the Madden-Julian Oscillation (MJO) impact the South American continental slope through atmospheric and oceanic teleconnections (e.g., Conejero et al., 2020; Madden & Julian, 1994; Sprintall et al., 2020). Equatorial Kelvin Waves, forced by large scale wind stress anomalies, travel eastward and reach the western American coast where part of their energy excites weakly dissipative TWs which propagate southward along the continental slope (Clarke & Shi, 1991; Kessler et al., 1995; Roundy & Kiladis, 2006; Sprintall et al.,2020). Indeed, propagation of sea level and along-shore velocity anomalies along the Pacific side at subseasonal periods (50, 70, and 120 days) have been documented (e.g., Clarke & Ahmed, 1999; Pizarro et al., 2001). The observed TWs had speeds comparable to the first and second mode of coastal Kelvin waves (order of 2 m/s) and spatial structures consistent with those predicted by linear theory (Brink, 1982; Illig et al., 2018).

On the Atlantic side, local wind anomalies over the southern Patagonian platform and around 40°S trigger northward propagating shelf-break and coastal TWs with rather short periods ranging between 5 and 30 days (Freitas et al., 2021; Poli et al., 2020). Waves depart at distinct sites corresponding to abrupt changes in the shelf-break orientation (Poli et al., 2020). North of the Abrolhos Plateau (AP; 22°S) the width of the shelf reduces dramatically which makes this region a hotspot for wave energy dissipation (Freitas et al., 2021).

Signatures of lower frequency TWs have also been observed from in situ and satellite data and model outputs on the Atlantic side. Vivier et al. (2001) observed energetic peaks at intraseasonal timescales (between 50 and 110 days) in velocity spectra from current meter mooring data, located at 41°S on the Atlantic continental slope.

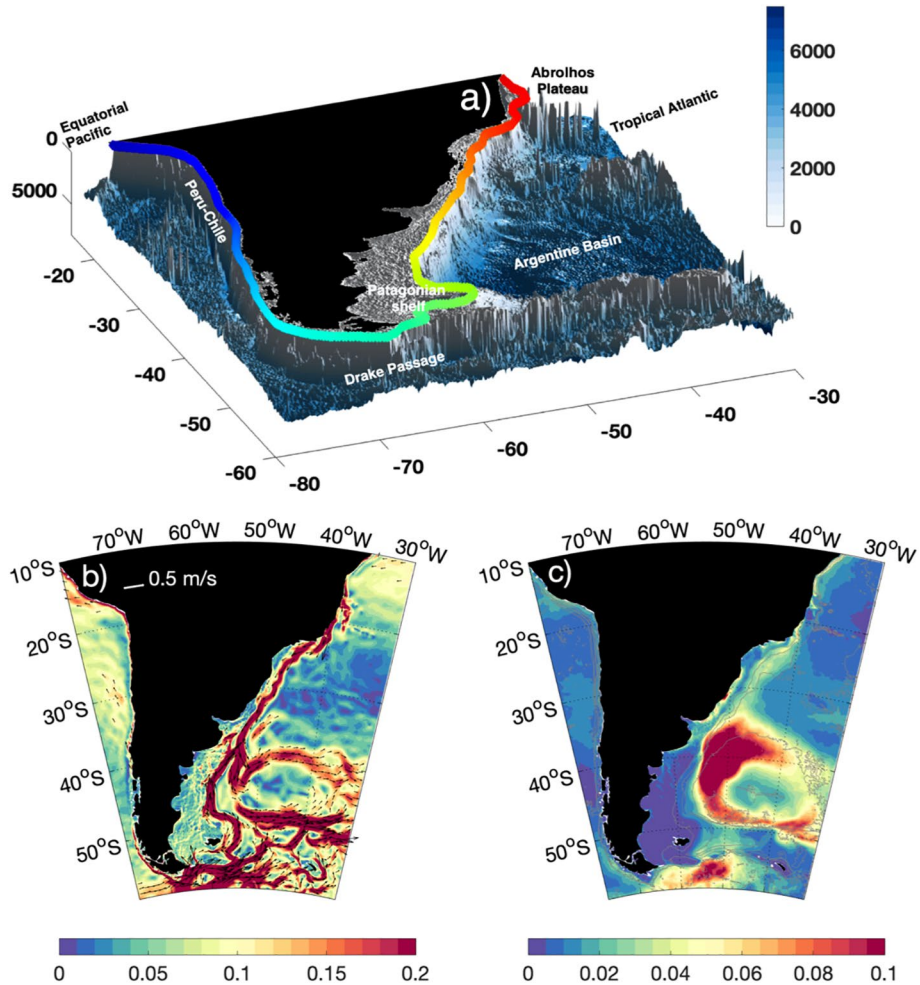

Figure 1. (a) Bathymetry (in m) used in GLORYS12. The colored track follows the 300 m isobath marking the shelf break. (b) Mean surface velocity (m/s) (arrows and amplitude in color). The arrows corresponding to velocities larger than 10 cm/s are from GLORYS12 over 1993–2019. (c) Mean eddy kinetic energy (m^2/s^2). Isobaths 6000, 5000, 3000, 2000, 300 are indicated in gray.

They suggested that those peaks could be related with TW propagating from the Pacific following the southern edge of South America and continuing their propagation in the Atlantic along the Patagonian slope. Hughes and Meredith (2006) identified strong coastal satellite sea level anomalies (SLA) correlations between the eastern and western side of South America resulting from the propagation of TWs from the Equatorial Pacific (EP) to the Patagonian shelf. Combes and Matano (2019) investigated the influence of remote wind forcing on low frequency (periods ≥60 days) SLA over the Patagonian platform with model experiments. They highlighted the influence of EP dynamics and winds along the southern Chilean coast in forcing SLA on the Patagonian Platform through TWs.

Modifications of the TW structures are expected along the propagation due to changing background. Indeed, the South American Pacific and Atlantic sides present contrasted characteristics regarding seafloor topography (Figure 1a) and ocean circulation (Figures 1b and 1c). The Pacific coast has a quasi-meridional orientation and the continental slope is steep (100 m/km) north of 38°S (subduction zone with a fault reaching 6,000 m depth) and more gentle (60 m/km) to the south. On the Atlantic side, the continental platform is wide in the south (1,000 km wide at 50°S) and very narrow to the north of 22°S. The shelf break is rather sinuous and the continental slope gentle in the southern part (20 m/km around the Malvinas Islands) and steeper (50 m/km) north of 46°S. Currents along the Pacific slope, the northward Humbolt Current north of 42°S and the poleward Cape Horn Current south of 45°S, are rather weak, seasonally varying with mean velocities of the order of few cm/s (e.g.,

Strub et al., 2019). In contrast, the western boundary currents on the Atlantic side are strong with the Malvinas Current (MC), an emanation of the Antarctic Circumpolar Current, flowing northward with surface velocities reaching 0.6 m/s and the poleward Brazil Current with surface velocities of 0.3 m/s (Figure 1b). The encounter of these two currents around 40°S generates strong eddy kinetic energy ($\geq$0.1 m^2/s^2, Figure 1c) making the western Atlantic one of the most energetic region of the world's oceans. In contrast the eddy kinetic energy on the Pacific side is rather weak ($\leq$0.01 m^2/s^2; Figure 1c).

We aim at revisiting TWs propagating around South America focusing on the propagation and evolution and investigating the forcing mechanisms. We take advantage of the 27 years global ocean reanalysis GLORYS12 which provides a tridimensional view of the ocean state. Previous works have assessed the performance of GLORYS12 in the MC system and in the Drake Passage (DP) and showed the skills of the reanalysis in reproducing the circulation and the hydrography of the region (Artana et al., 2018, 2019; Poli et al., 2020). In Section 2 we present the GLORYS12 reanalysis which we further validate comparing model SLA with observations from tide gauges located around South America. We present the linear theoretical model (Brink, 1982) which provided guidance for our study. In Section 3, we explore the sea level spectral content around South America and the propagation characteristics of the waves. Section 4 investigates the wave occurrences, the forcing mechanism, the vertical structure and the impact on along-shore velocities around South America. Section 5 summarizes and concludes.

2. Data and Method

2.1. GLORYS12 Reanalysis

The high-resolution (1/12°) global Mercator Ocean reanalysis (hereafter GLORYS12) has been developed in the framework of the Copernicus Marine Environment Monitoring Service (CMEMS, http://marine.copernicus.eu/) and covers the period from 1993 to 2019 (Lellouche et al., 2021). The ocean surface is forced by the global ERA-Interim atmospheric reanalysis from the European Center for Medium-Range Weather Forecasts. The model assimilates observations using a reduced-order Kalman filter with a 3-D multivariate modal decomposition of the background error and a 7-day assimilation cycle (Lellouche et al., 2021). The model assimilates jointly along track satellite altimetric data, satellite sea surface temperature, sea-ice concentration, and in situ temperature and salinity vertical profiles (Lellouche et al., 2021). Artana et al. (2018) evaluated the performance of the reanalysis GLORYS12 over the MC and found a good agreement with observations. We further examine GLORYS12 performance comparing GLORYS12 SLA with tide gauges and satellite altimetric data. Daily filtered tide gauges data were downloaded from the sea level center of the University of Hawaii (http://uhslc.soest.hawaii.edu/data/) and the daily satellite data is the delayed time multi-satellite gridded product (with a grid spacing of 1/4°) produced by Ssalto/Duacs and distributed by CMEMS (http://marine.copernicus.eu/). The maps are produced using an optimal interpolation method applied to altimeter observations (Pujol et al., 2016). Due to the filtering properties the effective temporal resolution is not 1 day, rather 20 days and the effective spatial resolution in mid-latitudes is 200 km (Ballarotta et al., 2019).

We show comparisons for the years 2015–2016 which feature the largest tide gauge data return. Those years correspond to a period of high ENSO activity. We computed the SLA standard deviations (stds), The correlation and root mean square error (corr and rmse) between tide gauges and GLORYS12 time series and between tide gauges and satellite altimetry time series (Table 1). Tide gauges data are not assimilated in GLORYS12. Collocalized GLORYS12 SLA are well correlated with tide gauge data (above 0.5 above 99% significance level, Table 1) and match tide gauge data better than collocalized satellite altimetry product does (larger correlation [corr] and smaller root-mean-square error [rmse], Table 1). GLORYS12 SLA time series feature smaller stds than the tide gauges suggesting that the signal amplitude is in general underestimated by about 20%–40% in GLORYS12 (Table 1).

As an example, GLORYS12 SLA provides a spectrum at Arica with similar peaks to the tide gauge data spectrum in the period range 10–50 days whereas satellite altimetry spectrum shows discrepancies in the energy peak locations (Figure 2b). Distance-time SLA diagram along a track following the 300 m isobath show coherent SLA patterns around South America (Figure 2c). Correlations between GLORYS12 SLA signal on the track and the nearest tide gauge are still significant above 99% on the Pacific side and decrease on the Atlantic side probably

Table 1
Statistics of the Comparison Between GLORYS12 SLA, Satellite Altimetry and Tide Gauge Data at the Tide Gauge Location

	GLORYS12			Altimetry		
Tide Gauges (std in m)	corr	rmse (m)	std (m)	corr	rmse (m)	std (m)
Arica (0.06)	0.88	0.03	0.05	0.46	0.05	0.04
Antofagasta (0.06)	0.80	0.04	0.04	0.6	0.05	0.03
Caldeira (0.05)	0.80	0.03	0.04	0.62	0.04	0.03
Valparaiso (0.06)	0.66	0.04	0.04	0.36	0.05	0.04
Puerto Mont (0.08)	0.37	0.07	0.04	0.13	0.08	0.04
Ushuaia (0.17)	0.60	0.13	0.06	0.41	0.15	0.06
Puerto Madryn (0.18)	0.50	0.17	0.17	0.26	0.19	0.12
Mar del Plata (0.23)	0.78	0.10	0.17	0.32	0.20	0.08

due to the large shelf width in the south (not shown). The coherent SLA patterns observed in GLORYS12 are somewhat blurred in the satellite SLA distance-time diagram (Figure 2d).

2.2. Modal Structures of Trapped Waves From Linear Theory

Trapped Waves under the long wave assumption (sub-inertial frequencies and along-shore scales larger than the shelf width), can be described as a sum of modes whose spatial structure, phase and group velocities depend upon the cross-shore topography, stratification and mean flow (Brink, 1982). The structure of the waves depends on the Burger Number Bu= $\frac{\alpha^2 N^2}{f^2}$, with α the bathymetry gradient, N^2 the mean Brunt-Väisälä frequency averaged in the vertical and f the Coriolis parameter (Huthnance, 1978). The Burger number expresses the ratio between density stratification in the vertical and earth's rotation in the horizontal. $Bu < 1$ indicates barotropic dynamics and $Bu > 1$ baroclinic dynamics. The phase speed and vertical characteristics of the waves depend upon the baroclinicity. Brink (2018) considered a linear, inviscid problem with constant rotation, horizontally uniform stratification (N(z)), and an along-shore non-varying bottom topography (h(x)). Brink and Chapman developed a toolbox that computes modal structures from bottom topography h(x), offshore stratification N^2(z), mean flow (V (x, z)), for a given frequency and wavenumber, by resolving the linearized primitive equations (available at: https://darchive.mblwhoilibrary.org/handle/1912/10527). The dispersion curves and the wave structures were examined at four sections: at PN located at 25°S and PS at 50°S on the Pacific side and AS at 47°S and AN at 31°S on the Atlantic side (Figure 3a). The three first gravest modes are shown in Appendix A.

2.3. Climate Indices: El Niño Southern Oscillation (ENSO) and Madden-Julian Oscillation (MJO)

We use the detrended ENSO index (Niño 3.4) available at https://psl.noaa.gov/data/correlation/nina34. data El Niño or La Niña events are defined when the Niño 3.4 SSTs exceed ±0.4°C for a period of 6 months or more.

We also use the Original OLR MJO Index (MJO OOMI) available at https://psl.noaa.gov/mjo/mjoindex/. The index is a projection of 30–96 days eastward-only filtered OLR onto the spatial EOF patterns of 30–96 days eastward filtered OLR. This index indicates the activity and the phase of the oscillation (Kiladis et al., 2014).

2.4. ERA-Interim

We use winds (U10m and V10m) from ERA-Interim global atmospheric reanalysis provided by the European Center for Medium Range Weather forecast available at https://www.ecmwf.int/en/forecasts/datasets/reanalysis-datasets/era-interim. The system includes a four-dimensional variational analysis (4D-Var) with a 12-hr analysis window for the assimilation. The spatial resolution is approximately 80 km with 60 vertical levels in from the surface to 0.1 hPa (Dee et al., 2011).

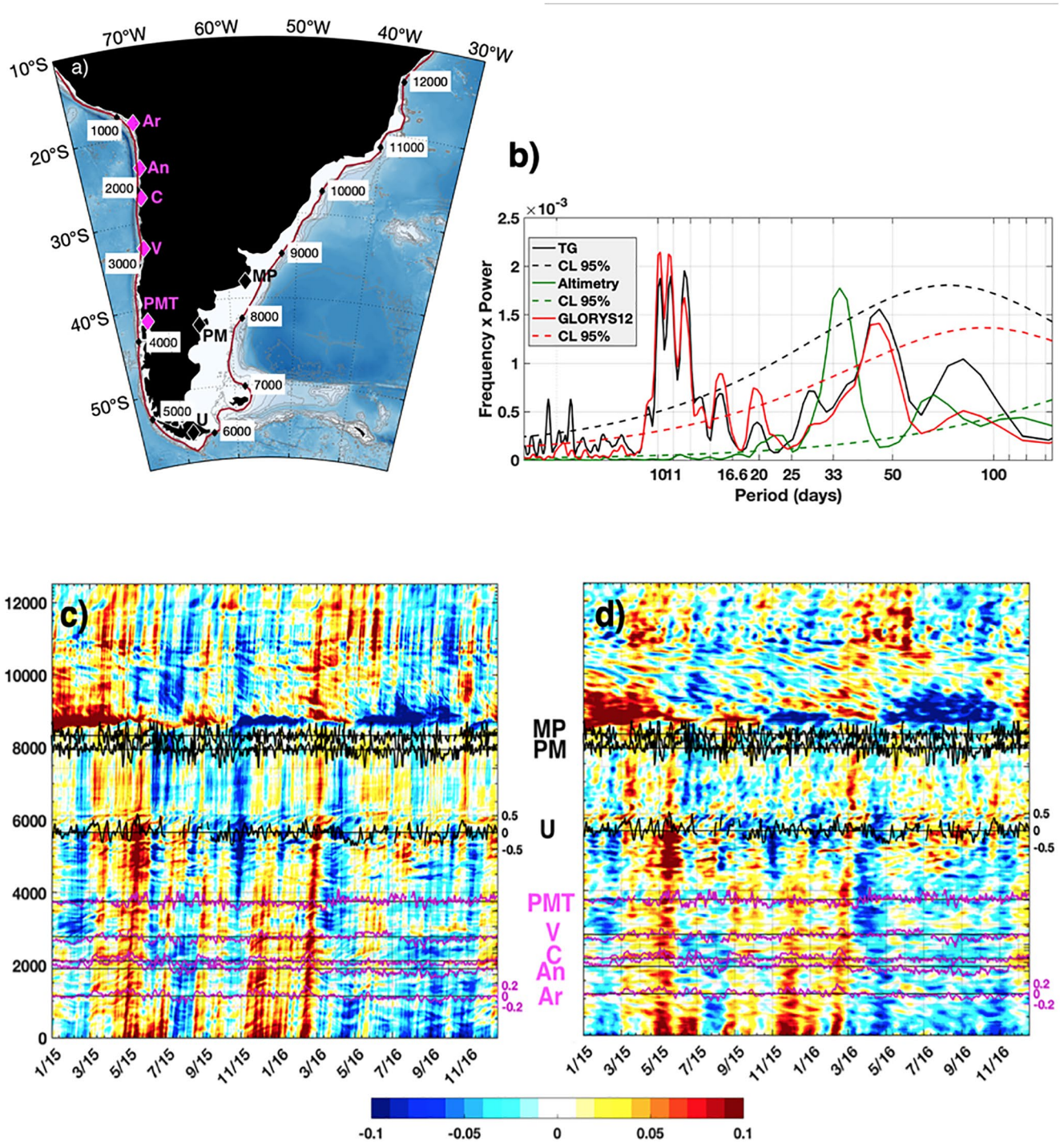

Figure 2. (a) Track along the 300 m isobath (brown curve) and tide gauge locations on the South American coastline. (b) Variance preserving spectra of SLA from GLORYS12, tide gauge (TG) and satellite altimetry at Arica. Dashed lines correspond to 95% confidence level (CL). Y-axis in m^2. (c) SLA distance-time diagram along the 300 m isobath from GLORYS12 for the period 2015–2016. X-axis is time (mm/yy) and Y-axis distance in kilometer along the track. Black (Atlantic side) and magenta (Pacific side) curves correspond to tide gauge data time-series with secondary y-axis (to the right) in meter. Magenta y-axis for Arica (Ar), Antofagasta (An), Caldeira (C), Valparaiso (V), Puerto Mont (PMT), and the black y-axis for Ushuaia (U), Puerto Madryn (PM), and Mar del Plata (MP). (d) Same as (c) for SLA satellite altimetry data.

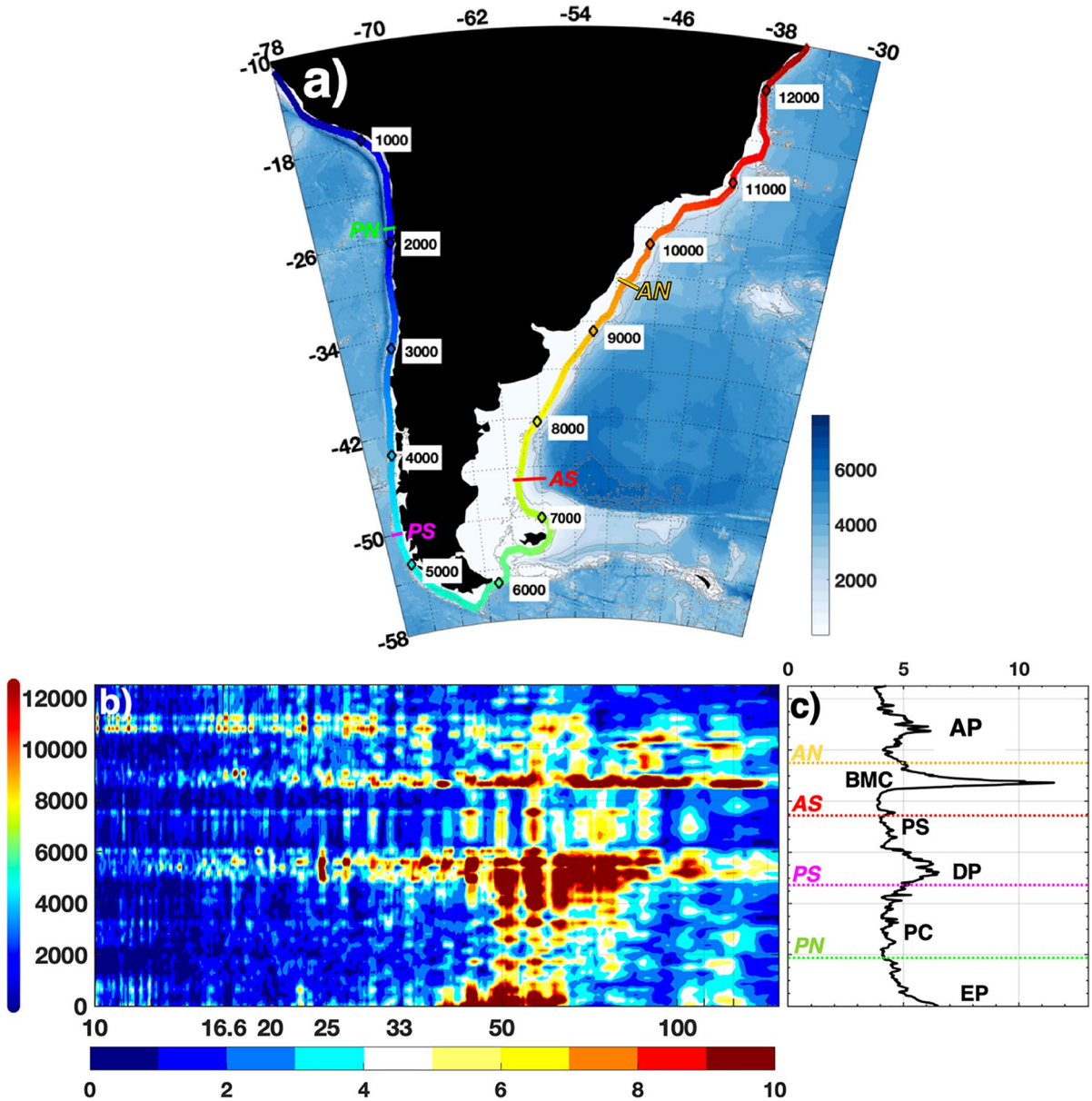

Figure 3. (a) Bathymetry (in m) and track following the South American shelf break (300 m isobath). Labels along the track indicate distance from 10°S to 78°W (off Peru). (b) Period – distance spectrum for SLA along the track around South America (bottom colorbar in cm^2). The colored line to the left of the y-axis indicates the position along the track (same colors as Figure 3a). Y-axis is distance along the track in kilometer and x-axis periods in days (log scale). (c) Standard deviation of sea level along the track (y-axis as in (b)) and x-axis in cm. PN, PS, AS, and AN correspond to the location of the four sections indicated in (a). EP, PC, DP, PS, BMC, and AB stand for Equatorial Pacific, Peru-Chile, Drake Passage, Brazil-Malvinas Confluence, and Abrolhos Plateau respectively.

3. Coherent SLA Propagation Around South America: 27 Years Overview and Statistics

3.1. Spectral Content

We examined the spectral content of SLA following the 300 m isobath (Figure 3a) and focused on the 10-150-day period range (Figure 3b). Four regions stand out in the spectrum: the EP (0 km), the DP (5,000–6000 km), the Brazil-Malvinas Confluence (BMC, 8,500–9,000 km), and the AP(11,000 km; Figures 3b and 3c).

The energy at periods shorter than 30 days between 6,000 and 8,000 km is associated with locally wind-forced TWs propagating northward along the Patagonian shelf documented by Poli et al. (2020) and between 10,000

and 13,000 km with those documented by Freitas et al. (2021). The SLA spectrum shows coherent energy peaks at periods ranging between 40 and 130 days all along the 300 m isobath. The energy is larger at DP and at the BMC where the SLA std along the 300 m isobath shows large peaks (Figures 3b and 3c). The coherent patterns between 40 and 130 days in Figure 3b suggest teleconnections between EP and Tropical Atlantic through TWs.

SLA wavelength-period spectra were produced considering the whole track following the 300 m isobath (Figure 4a). The spectrum indicates a cyclonic propagation of waves that is with the coast to the left (Figure 4a). The energy is particularly concentrated at periods between 40 and 130 days and wavelengths between 6,000 and 12,000 km. Energy peaks are consistent with theoretical modal dispersion curves computed with Brink's toolbox for the AS, AN, PS, and PN sections of Figure 3.

AS shows the largest phase speeds while the lowest ones are found on the Pacific side at PN. Therefore in Figure 4a we show the theoretical dispersion curves corresponding to the three gravest modes of these two extreme cases (AS in red and PN in green). The theoretical dispersion curves at PS and AN are located between those of PN and AS. Phase velocities range between 2 and 7 m/s for mode 1, between 1.4 and 3 m/s for mode 2, and between 1 and 1.5 m/s for mode three.

The difference in phase speeds reflects distinct background characteristics such as slope steepness and stratification. Indeed, the Burger number (Bu, Figure 4b) quantifies the impact of those parameters on the baroclinicity of the wave, when $Bu > 1$ the wave is expected to be baroclinic and when $Bu < 1$ barotropic. The theory predicts faster propagation for barotropic waves.

Figure 4b suggests a rather baroclinic structure on the Pacific side of South America and on the Atlantic side to the north of 38°S and a barotropic structure in the south of the Patagonian platform. This is consistent with theoretical phase speeds. The continuity of energy peaks between 40 and 130 days shown in Figure 3 and the contrasting phase velocities (Figure 4a) around South America could be indicative of an energy transfer between modes induced by the changing slope steepness and orientation, stratification and mean flow along the path (Figures 1 and 4b).

3.2. Coherent Propagative SLA Patterns and Their Phase Speeds

To isolate the low frequency waves propagating around South America we band-pass filtered model outputs between 40 and 130 days. Lagged correlations between a 27-year-long time series of filtered SLA at 60°W 47°S (300 m isobath at AS) and the SLA field show a coherent propagative signal coming from the EP (Figure 5). Lag 0 and lag −30 days show similar patterns with opposite signs suggesting a period of about 60–70 days and wavelength of about 12,000 km (Figure 5). The correlation reduces drastically at 22°S indicating a hotspot of wave energy loss probably associated with the abrupt change of the coast orientation near the AP.

We computed the Burger number (Bu) as well as the shelf width along the path (Figure 6a) and lagged correlations between 27-year-long time series of filtered SLA collocated along the track and SLA time series at PN (Figure 6b), PS (Figure 6c), AS (Figure 6d), and AN (Figure 6e). The lagged correlations show similar propagation patterns with a period of about 60/70 days. The wave periods are slightly shorter at the southern sections AS and PS (about 60 days) and larger at AN and PN (about 66 days) probably due to changes in the Coriolis parameter (Figure 6f). Propagation speed ranges from 1.8 m/s to 2.8 m/s between the EP (0 km) and DP (6,000 km). The wave then accelerates along the Patagonian shelf reaching speeds of about 4–7 m/s and then slows down to 1.8 m/s after the BMC. Interestingly Figures 6b–6d show a blurred signal and a decay in the correlation to the north of AN indicating that waves propagating from the Pacific strongly attenuate around 11,000 km. In contrast, correlations in panel d reflect a net northward propagating pattern with phase speed of 1.8 m/s to the north of AN. These correlations to the north of AN suggest a local wave forcing around AN (Figure 6e).

Bu is less than one (Figure 6a) along the Patagonian slope, where waves propagate faster, and exceeds one elsewhere where waves are slower, which is consistent with theory. Theory also predicts faster propagation speed over larger continental shelf as observed along the Patagonian platform where the width exceeds 500 km (Figure 6a).

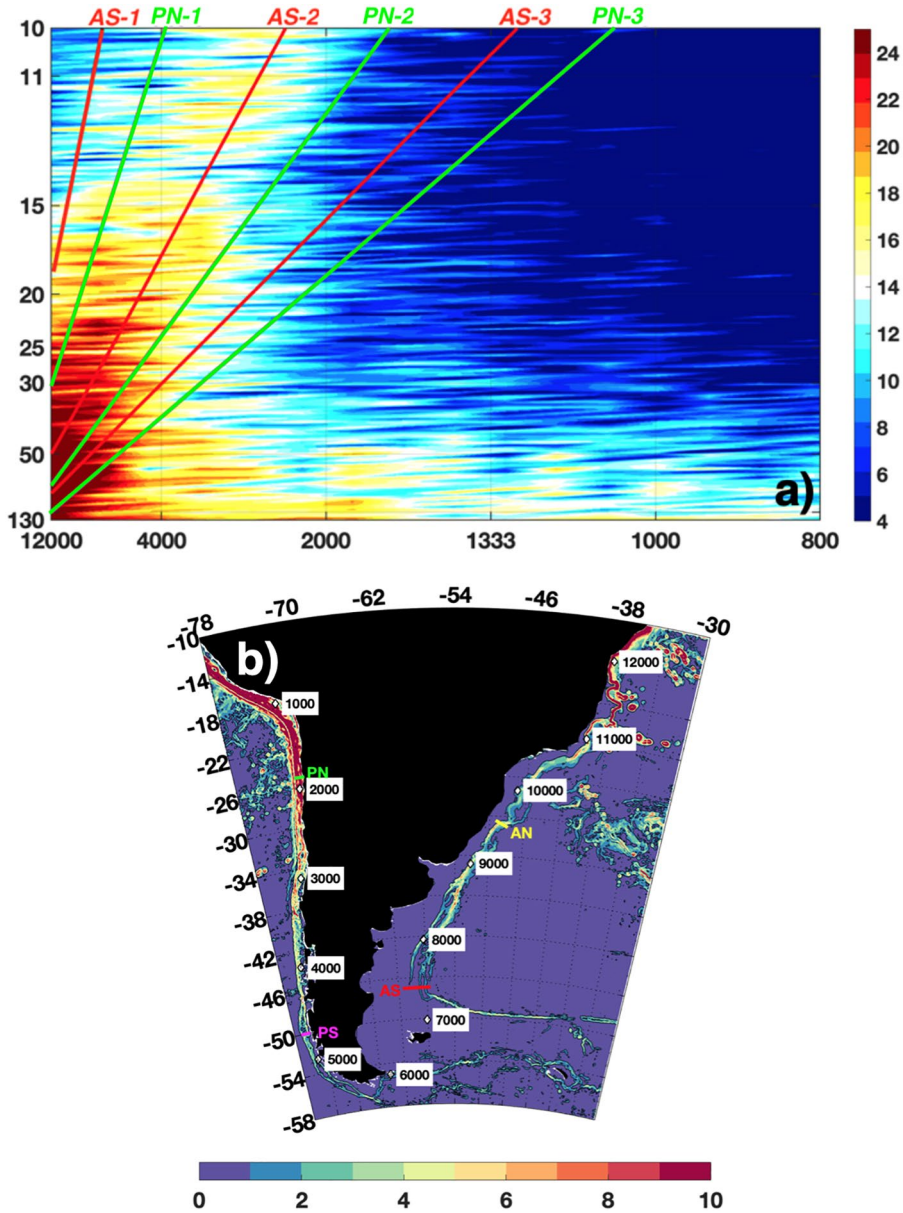

Figure 4. (a) SLA wavelength-period spectrum for the entire track over 27 years. X-axis is wavelength in kilometer and y-axis periods in days. The curves represent the theoretical dispersion relations for the first three gravest modes at PN (green) and AS (red) sections computed with Brink's toolbox (cf. Section 2.2). Colorbar units: SLA power spectral density. (b) Mean Burger number ($\frac{\alpha^2 N^2}{f^2}$ with α the slope, N the vertically averaged Brunt Väisälä frequency and f the Coriolis parameter) from GLORYS12 over the 1993–2019 period. Black contour is Bu = 1.

4. Trapped Waves Evolution Around South America

4.1. Waves Occurrences and Climate Indices

Figure 7a presents a distance-time diagram along the track following the 300 m isobath of filtered SLA from 1993 to 2019. Striking features are the intermittent coherent SLA propagative patterns from 0 to 12,000 km. Between 3,000 and 6000 km the SLA signal is more continuous in time suggesting a local reinforcement. The SLA signal associated with the BMC clearly appears at 9,000 km. Several propagative SLA signals seem to be generated intermittently at the Confluence (e.g., in 2010) possibly corresponding to the signal seen to the north of AN in Figure 6e.

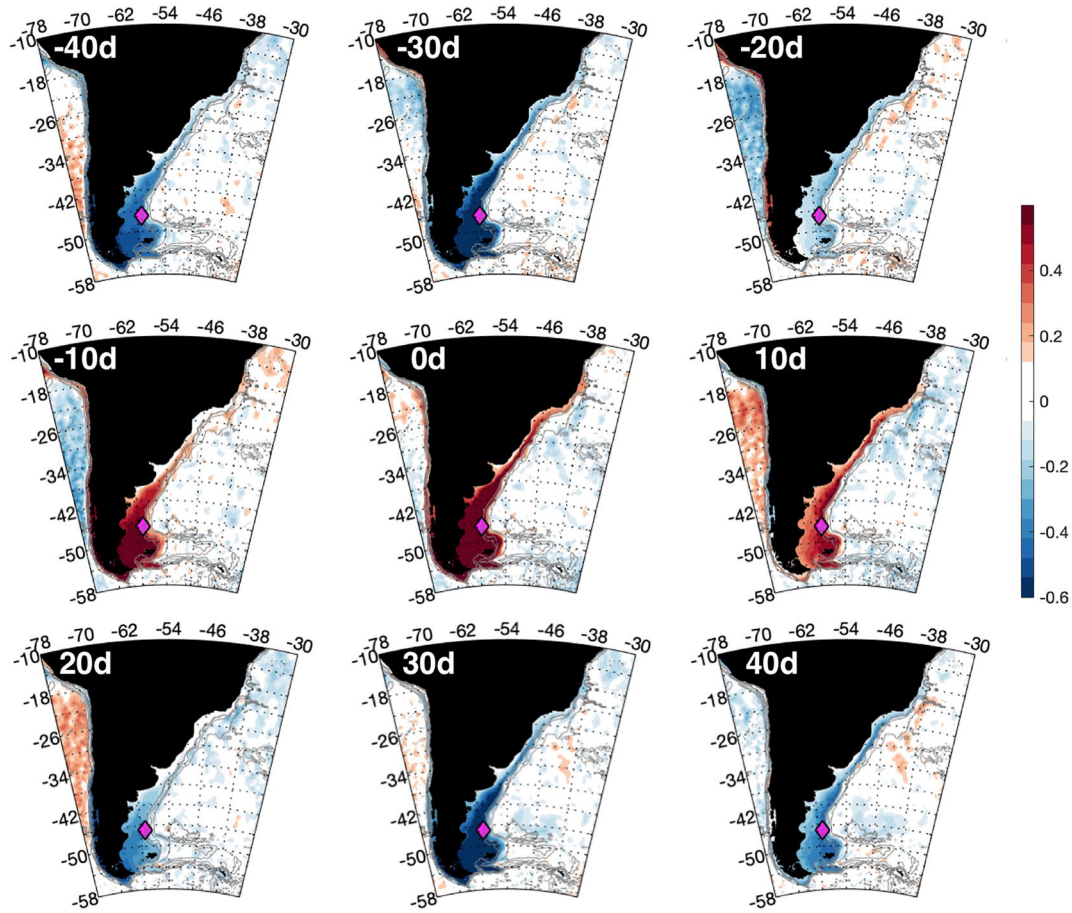

Figure 5. Lagged correlation of SLA with SLA time series at 47°S 60°W (magenta diamond on AS section) for the period 1993–2019. SLA was band-pass filtered between 40 and 130 days. Lags are indicated in white. Only significant correlations are colored.

We produced envelopes of filtered SLA intensity time series at the intersection of the sections and the 300 m isobath (Figure 7b). The envelopes were computed using smoothing a spline method. The envelopes can be considered as a proxy of the wave activity (Roundy & Kiladis, 2006). Most of the time the envelopes at PN, PS, AS, and AN are in phase. The amplitude at PS is generally larger (in pink in Figure 7b) corresponding to the intensified signal mentioned above. At times, the signal is larger at AN (in yellow in Figure 7b; e.g., in 2010) as observed in Figure 7a.

The envelope time series seem to be modulated over time featuring larger values during the following periods: 1997–1998, 2002–2005, 2009–2010, 2015–2016 and 2019, corresponding to El-Niño periods as illustrated with El Niño 3.4 index in Figure 7c.

The strong wave activity around South America starts before the El Niño episodes which is consistent with equatorial kelvin waves preceding (and generating) El Niño events (Hendon et al., 1998; Kessler & Kleeman, 2000; McPhaden, 1999; Roundy & Kiladis., 2006). The wave activity around South America lasts during each El Niño period. Therefore the El Niño phenomena seem to modulate the wave activity at low frequency (>3 years).

The MJO (Madden & Julian, 1994) with a characteristic periods of 50 days is an important mechanism in the generation of Equatorial Kelvin waves (Roundy & Kiladis, 2006). Indeed, the OOMI index Amplitude time series (see Section 2.3) seems to mimic the SLA envelope time series (Figure 7d).

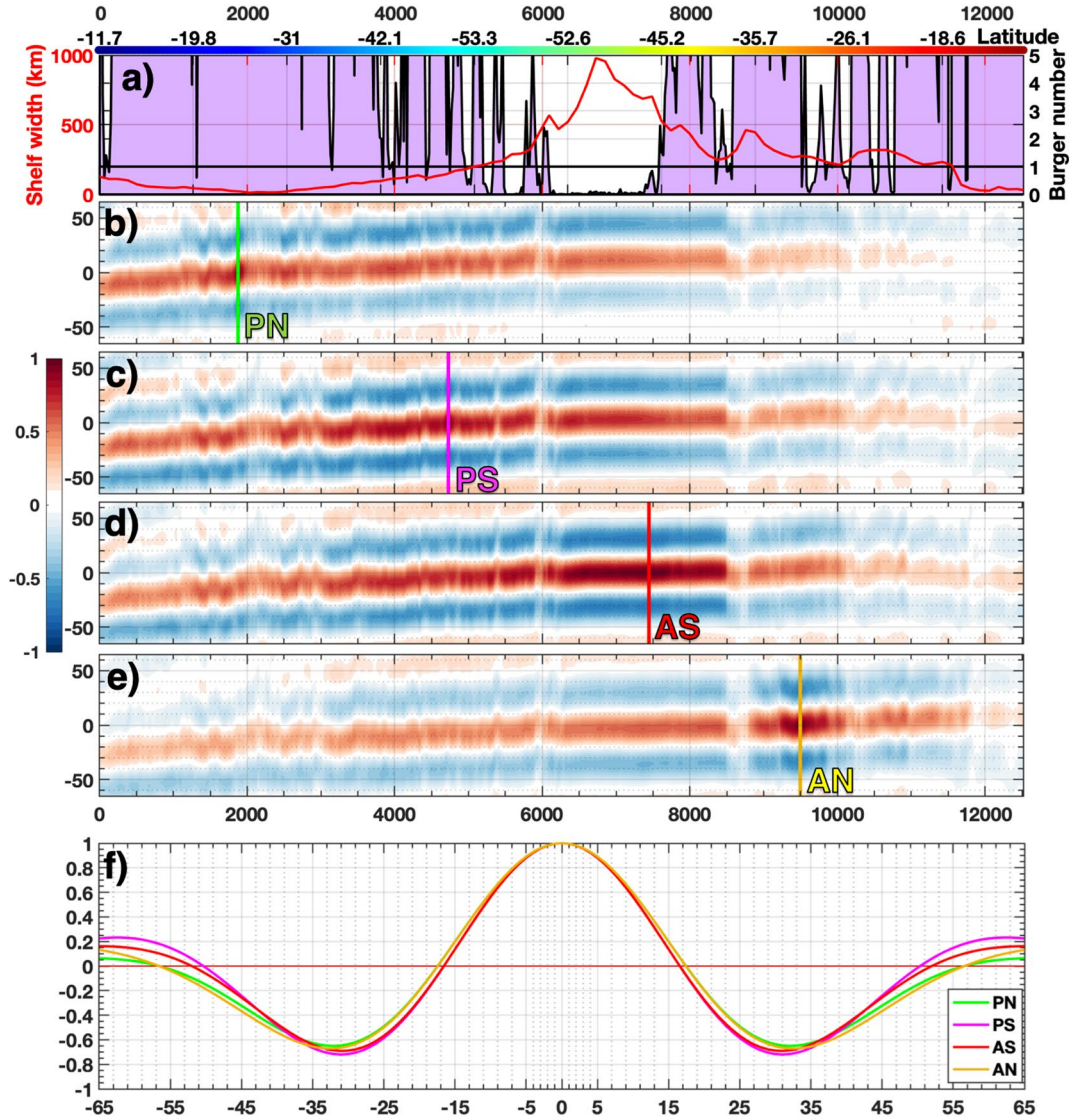

Figure 6. (a) Mean Burger number along the track in purple shade (black Y-axis on the right). Black line is Bu = 1. Red curve is shelf width in kilometer along the track (left red Y-axis). The colorbar indicates distance and latitude along the track as in Figure 3a. (b) Lag correlation diagram between SLA along the track and SLA at PN (27-year-long time series). (c) Same as b for SLA at PS. (d) Same as b for SLA at AS. (e) Same as b for SLA at AN. Only significant correlations are colored. A linear fit of maximum correlations provide estimates of the phase velocities. (f) Lagged correlations for each section (PN, PS, AS, and AN). X-axis is lag in days and y-axis correlation coefficient. 95% confidence level is 0.1. All SLA time series were band-pass filtered between 40 and 130 days.

We produce lagged correlation-distance diagram between 40 and 130 day filtered SLA along the track and MJO OOMI index (PC1; Section 2.3) over the 27 years (Figure 8).

The correlations are significant, large (absolute value of $r \geq 0.3$) and coherent with the propagative patterns observed in Figure 6 (same phase speeds and periods). The maximum correlations are obtained at lag 30 days at EP (−10°S), lag 43 days at PN, lag 56 days at PS and lag 60 days at AS and lag 63 days at AN. The lagged correlations suggest that the MJO plays a major role in forcing the waves propagating around South America. However, intensification and generation observed in particular at PS and AN (Figure 6), hint at local processes. We explore the role of local wind in the following section.

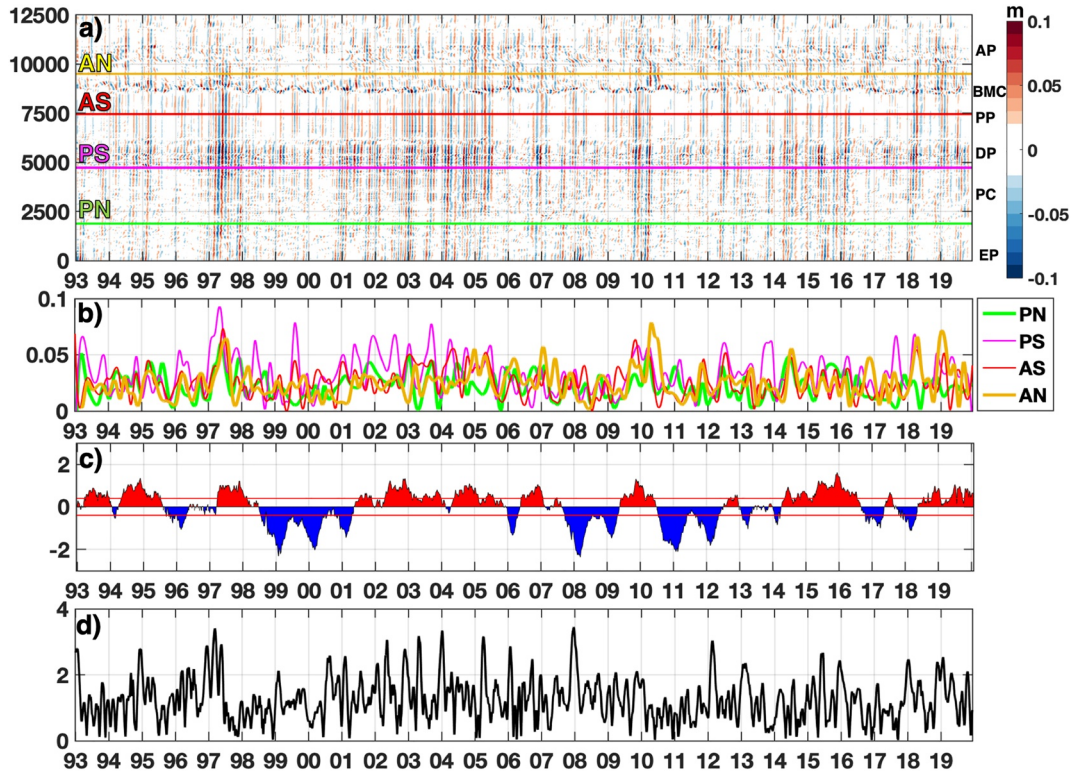

Figure 7. (a) Distance-time diagram of 40–130 days band-pass filtered sea level anomalies along the track following the 300 m isobath for the 1993–2019 period from GLORYS12. X-axis is time in years, Y-axis is distance along the track in kilometer. Color bar is SLA in meter. The four sections are indicated. (b) Envelope of filtered SLA amplitude at the location of the four sections in meter. (c) Detrended SST anomalies from El Niño 3.4 (in °C). (d) Original OLR Madden-Julian Index Amplitude (normalized – see Section 2.3).

4.2. Wind Forcing

Regression maps of the band-pass filtered SLA averaged around the southern tip of South America onto wind components were performed at many lags. Only regressions with the meridional component show conclusive results. Indeed, the regression maps of the band-pass filtered SLA averaged around the southern tip of South America onto the meridional component of the wind show a distinctive negative pattern (above 99% CL) around South America from lag −10 to 5 days. This pattern, maximum at lag −10 days (Figures 9a and 9b), moves westward and attenuates at lag 5 days (not shown).

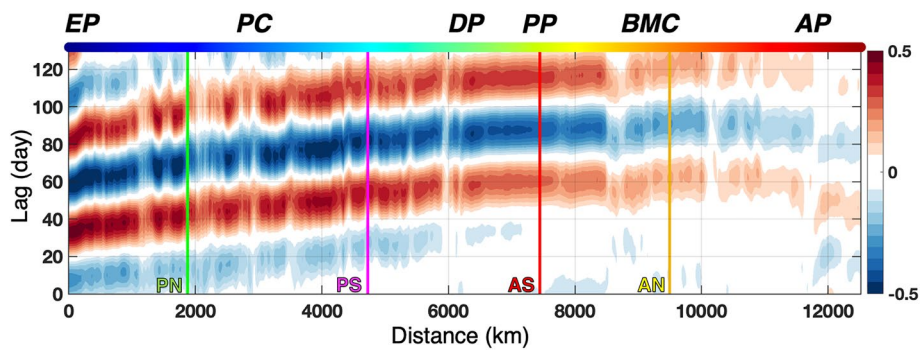

Figure 8. Lagged correlation-distance diagram between 40 and 130 day filtered SLA along the track following the 300 m isobath and MJO OOMI index (PC1) computed over 27 years (1993–2019). Y-axis is lag in days, X-axis is distance along the track in kilometer. The upper colorbar indicate the position along the track as in Figure 1a. PN, PS, AS, and AN locations are marked with vertical color lines.

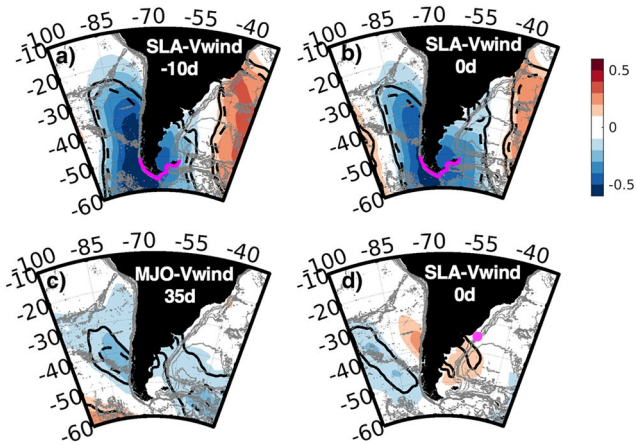

Figure 9. (a) Regression map of the band-pass filtered SLA averaged along the magenta line (around the southern tip of South America) onto the meridional component of the wind at lag −10 days. (b) Same as (a) for lag 0 days. (c) Regression map of MJO OOMI (PC1) index onto the meridional component of the wind for lag +35 days. (d) Regression map of the band-pass filtered SLA at the magenta dot (north of the BMC) onto the meridional component of the wind at lag 0 days. The thick (dashed) black lines are the 99 (95)% confidence level. Color scale in m/s.

This negative pattern corresponds to northerly winds which, through Ekman transport, increase the positive SLA signal along the Pacific coast and decrease the positive SLA on the Atlantic side. Thus the local meridional winds reinforce the wave amplitude on the Pacific side and reduce it on the Atlantic side. This explains why the observed SLA signal is stronger at PS than AS (Figure 7). Interestingly, the negative wind pattern shows up in the regression between the MJO and the meridional component of the wind at lag 35 days (Figure 9c). This suggests that the MJO forces TWs in two ways: through an oceanic connection implying equatorial Kelvin waves reaching PN at lag 43 days (Figure 8) and trough an atmospheric teleconnection enhancing northerly winds at lag 35 days and contributing to the reinforcement or generation of TWs along the southern Pacific coast. This implies that the atmospheric teleconnection reaches PS before the oceanic one. Most of TWs manage to cross the BMC and attenuate downstream (Figure 7a). As mentioned in the previous section, some waves seem to be locally generated at the confluence (Figure 6e). We therefore explore possible local wind forcing. The regression maps of the band-pass filtered SLA averaged north of the BMC (pink line at 35°S in Figure 9d) show a positive (southerly) wind pattern at lag 0 located at the confluence. This southerly wind could possibly force the TWs only observed north of the confluence in the Hovmöller diagram in Figure 7.

4.3. Wave Vertical Structure and Influence on the Mean Flow

The mean flow on the Pacific slope shows a rather baroclinic structure (PN and PS) with weak southward currents (core of 0.1 m/s; Figure 10, upper two panels of the first column). In contrast, the strong MC flows along the Patagonian slope with a barotropic equivalent structure and is organized in two jets with mean cores velocities of 0.2 m/s and 0.6 m/s at AS (Artana et al., 2021). Further North, at AN, the flow shows a baroclinic structure with mean southward surface velocities of 0.3 m/s of the Brazil Current above a northward flow at 700 m (Figure 10, lower two panels of the first column).

To explore the vertical structure of the waves, we produced composites of filtered along-shore velocity anomalies (40–130 days) at the four sections corresponding to the positive phase of the waves (Figure 10, second column). The events are selected from dates when the filtered SLA is larger than two standard deviation at the 300 m isobath of each section. We applied the same procedure to compute the composite of the along-shore velocity anomalies corresponding to the negative phase of the waves (not shown) selected from dates with SLA lower than minus two standard deviations. These criteria selected 22, 23, 19, and 29 positive events and 25, 25, 24, and 18 negative events for PN, PS, AS, and AN, respectively. The composites of along-shore velocity anomalies of positive events and negative events feature similar patterns of opposite sign (not shown), suggesting that the criteria selected positive and negative phase of the waves.

The along-shore velocity anomaly composites feature a rather baroclinic structure at PN, PS, and AN and a barotropic structure at AS (Figure 10 second column). The associated velocity anomalies reach 0.1 m/s on the Pacific slope, decrease at AS ($\leq$0.05 m/s) and intensify to the north at AN ($\geq$0.15 m/s).

In their positive phase, the waves strengthen the rather weak southward surface mean flow at PN and at PS (from 0.05 m/s to 0.2 m/s), intensify the onshore jet of the MC current (between 0 and 100 km, from) at AS, and enhance the subsurface northward jet (between 50 and 100 km) at AN (Figure 10, third column).

Although Brink's model is too idealistic (e.g., Brunner et al., 2019) and requires several assumptions such as a straight coastline with similar slope bathymetry, which are not fulfilled along the path, it provided guidance to the interpretation of those waves. The spatial structures of the velocity composites are reminiscent of the theoretical modes (obtained with the Brink and Chapman toolbox - appendix): modes 1–2 for the Pacific side, 2–3 at the AS and modes 1–2 at AN (Figure 10, second column). As mentioned before, dispersion curves for modes 1, 2, and 3 provided theoretical phase speed that match the observed ones (ranging between 1.2 m/s and 2.4 m/s on the Pacific slope and between 1 and 7 m/s on the Atlantic slope, Figure 4).

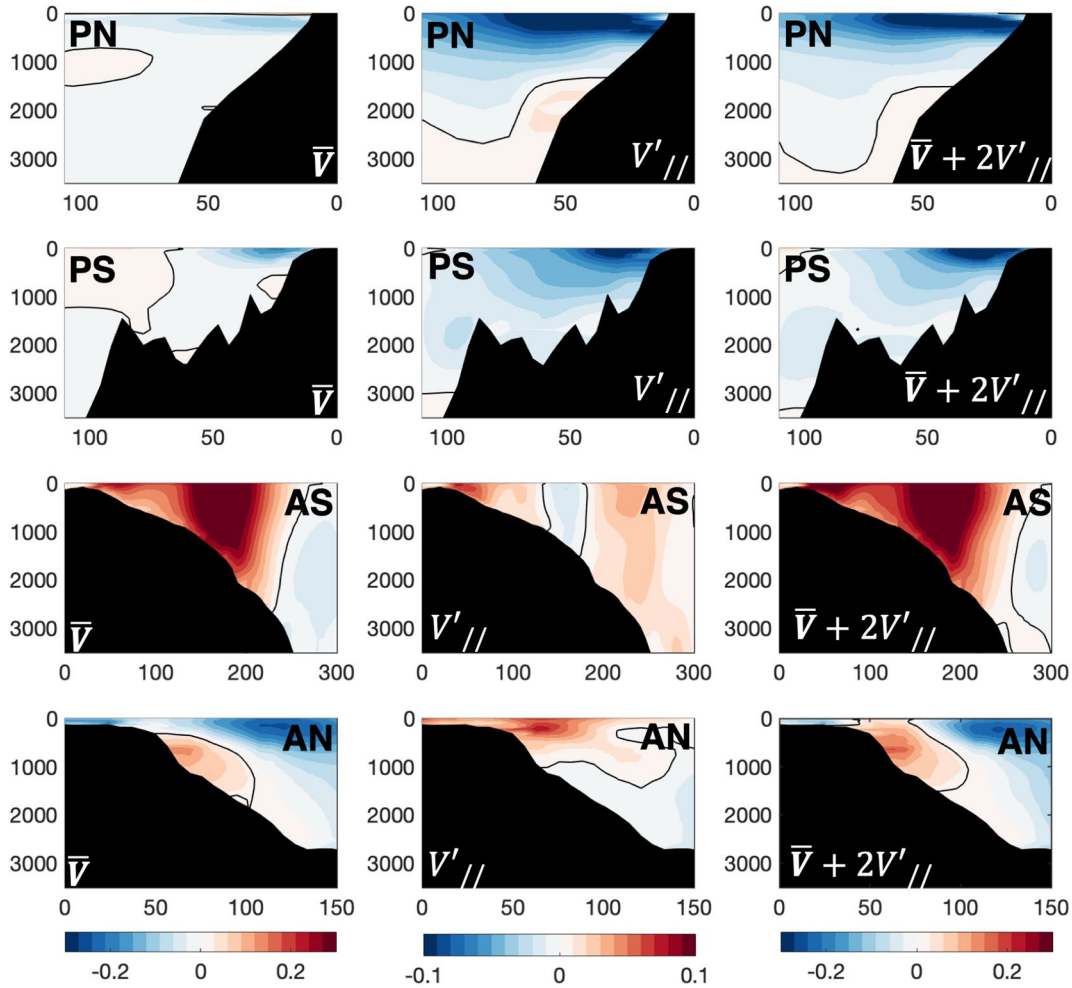

Figure 10. Left panels: 27-year mean along-shore velocities at the four sections. Central panels: composites of filtered along-shore velocity anomalies for the positive phase of the waves at the four sections PN, PS, AS, and AN. The composites are built from events selected when the SLA peak is larger than two standard deviations. Right panels: Along-shore velocities corresponding to positive phase of the waves (mean plus twice the anomalies). Scales in m/s.

5. Summary and Discussion

Sea level anomalies from GLORYS12 reanalysis reproduced well the signal measured by tide gauges around South America. The reanalysis better match the tide gauges signal than satellite altimetry data product which features blurred patterns (Figure 2). The 27-year-long global ocean reanalysis GLORYS12 documented waves with wavelengths between 8,000 and 12,000 km (Figure 5) and periods of 40, 50, 60, 70, and 110 days (Figure 3) propagating from the EP to the Tropical Atlantic (22°S) around South America (red arrows in Figure 11). The AP at 22°S is a hotspot for wave energy dissipation (Freitas et al., 2021).

Propagation speeds range from 1.8 to 2.8 m/s along the Pacific continental slope and from 1.8 to 7 m/s along the Atlantic slope. As predicted by theory, phase speeds are larger along the Patagonian Platform (5–7 m/s) as the shelf width is large and the Burger number small (Figures 4b and 6a). During their propagation, the waves encounter distinct background characteristics which affect their vertical structures. Indeed, on the Pacific side and off Brazil (PS, PN and AN) the waves have a baroclinic structure, whereas the structure is rather barotropic at AS. The phase speeds and the spatial structures across the slope at PN, PS, and AN correspond to theoretical modes 1–2 and to mode 2–3 at AS (Figures 10 and 4).

The MJO, through oceanic and atmospheric teleconnections, plays a key role in forcing the TWs. On one hand, the MJO forces Equatorial Kelvin waves that propagate to the east and reach the coast after 35 days. They trig-

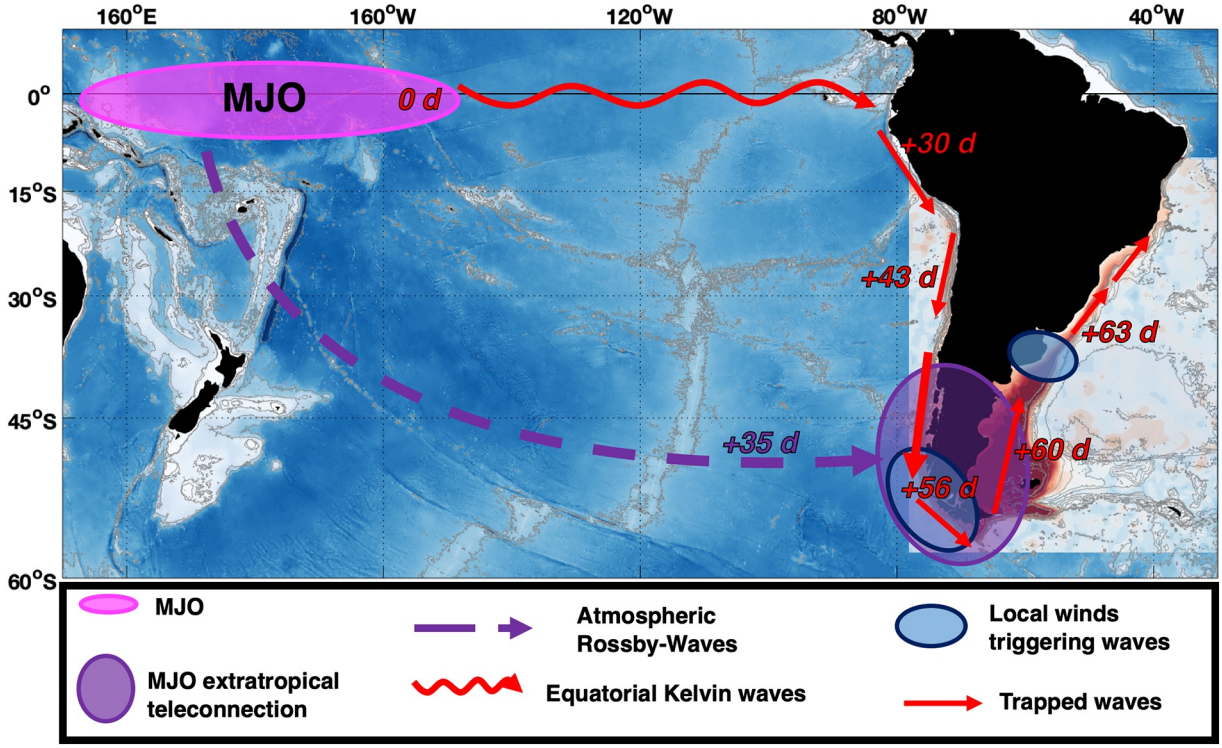

Figure 11. Schematics of mechanisms forcing trapped waves around South America. MJO is a key player in triggering trapped waves around South America through equatorial oceanic Kelvin waves (red) and atmospheric Rossby waves (dashed purple line). Lags (red) in days are deduced from the correlation between the MJO and the SLA over the track following the 300 m isobath. Lag in days (purple) are deduced from the regression between meridional winds and the MJO index, the associated wind signal is represented with the purple circle. Moreover, local wind forcing (in blue), not linked with the MJO, reinforce and/or generate trapped waves. For sake of illustration we superimposed the correlation at lag 0 days shown in Figure 5.

ger TWs that propagates poleward reaching PN 8 days later (lag 43 days with respect to MJO) and PS 21 days later (lag 56 days; Figure 8, red lines in Figure 11). This result is consistent with previous studies (e.g., Cravatte et al., 2003; Hendon et al., 1998; Illig et al., 2018; Roundy & Kiladis, 2006). On the other hand, the MJO also modulates TWs through an atmospheric teleconnection that reaches PS at lag 35 days (before the arrival of the oceanic teleconnection). Indeed the MJO trigger atmospheric Rossby waves that generate local wind anomalies over the southern tip of South America (purple dashed line in Figure 11; Berbery & Nogues-Paegle, 1993). The local wind anomaly pattern increases the wave amplitude at PS and decreases it at AS. The increasing in wave amplitude at PS could also be the consequence of topographic effects or wave reflection on the bottom.

The MJO amplitude is enhanced before El-Niño episodes. Trapped wave activity is larger before and during positive ENSO phases and ENSO seems to modulate the wave activity at low frequency (Figure 7). However, the linkage between MJO and ENSO is still controversial (e.g., Dewitte et al., 2007, 2008) and is out of the scope of this paper.

Trapped waves are also intermittently forced by local winds not necessarily related with the MJO, at specific locations such as Southern Chile and the BMC (blue circles in Figure 11).

Trapped waves impact the along-shore currents: during the positive phase of the waves the flow is enhanced by about 0.1 m/s at PN, PS, AS, and AN. The waves modulate the intensity of the MC inner jet at AS as discussed in Poli et al. (2020). At AN the mean flow exhibits a subsurface equatorward counter current, which is intensified and reaches the surface during the positive phase of the wave. The subsurface current deserves further study. The impact of the TWs on cross-shore, vertical velocities and other fields such as temperature or Chlorophyll-a are under investigation.

Appendix A: Trapped Waves Along Cross-Sections Around South America From Linear Theory

We compute TWs properties at the four sections located at 25°S (PN) and 50°S (PS) along the Pacific side and at 47°S (AS) and 31°S (AN) along the Atlantic side (Figure 3) using Brink's and Chapman toolbox (Brink, 2018). Following Poli et al. (2020), we used GLORYS12 outputs to estimate mean Brunt-Vaïsälä frequency and mean flow along the sections. Mean flows are shown in Figure 10. The mean flow along the Pacific side was small and neglected, while the "idealized" Brazil Current at AN comprised a southward jet and the Malvinas Current at AS comprised two jets (cf. figure A1 in Poli et al., 2020). The first three gravest modes shows structures highly dependent on Burger number (Section 3.1) and the slope steepness plays a major role (Figure A1). PN, PS, and AN modal structures present baroclinic characteristics, while AS modal structures are more barotropic. The dispersion curves are presented in Figure 4 of Section 3 and show faster velocities for barotropic-like modal structures than for the baroclinic ones.

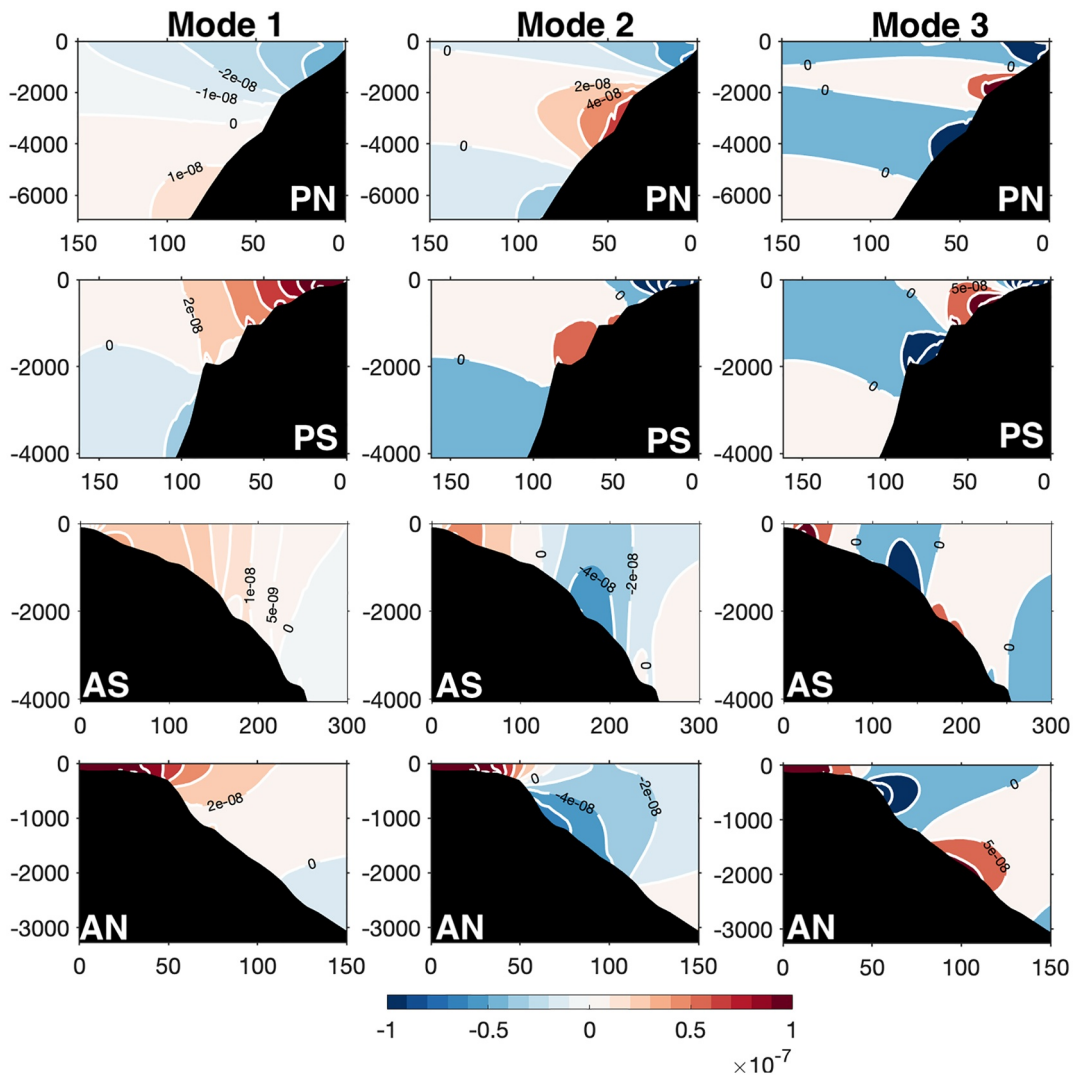

Figure A1. First three gravest mode computed with Brink and Chapman toolbox along the four sections.

Conflict of Interest

The authors declare no conflicts of interest relevant to this study.

Data Availability Statement

The satellite data and model outputs are available at Copernicus Marine Environment Monitoring Service (CMEMS; https://marine.copernicus.eu). ERA-Interim outputs are available at https://www.ecmwf.int/en/forecasts/datasets/reanalysis-datasets/era-interim. The climatic index are available at https://psl.noaa.gov/data/correlation/nina34. data for ENSO and at https://psl.noaa.gov/mjo/mjoindex/ for the MJO. Tide gauge data are available at http://uhslc.soest.hawaii.edu/data/.

Acknowledgments
We thank Jean-Michel Lellouche for his advice and help. We are grateful to CNES (Centre National d'Etudes Spatiales) for constant support. This study is a contribution to the CNES-funded BACI project. Léa Poli acknowledges support from Sorbonne Université and Camila Artana a CNES Postdoc Scholarship.

References

Artana, C., Lellouche, J.-M., Park, Y.-H., Garric, G., Koenig, Z., Sennéchael, N., et al. (2018). Fronts of the Malvinas current system: Surface and subsurface expressions revealed by satellite altimetry, Argo floats, and Mercator operational model outputs. *Journal of Geophysical Research: Oceans*, *123*, 5261–5285. https://doi.org/10.1029/2018JC013887

Artana, C., Provost, C., Lellouche, J.-M., Rio, M.-H., Ferrari, R., & Sennéchael, N. (2019). The Malvinas Current at the confluence with the Brazil Current: Inferences from 25 years of Mercator Ocean reanalysis. *Journal of Geophysical Research: Oceans*, *124*, 7178–7200. https://doi.org/10.1029/2019JC015289

Artana, C., Provost, C., Poli, L., Ferrari, R., & Lellouche, J.-M. (2021). Revisiting the Malvinas Current upper circulation and water masses using a high-resolution ocean reanalysis. *Journal of Geophysical Research: Oceans*, *126*, e2021JC017271. https://doi.org/10.1029/2021JC017271

Ballarotta, M., Ubelmann, C., Pujol, M. I., Taburet, G., Fournier, F., Legeais, J. F., et al. (2019). On the resolutions of ocean altimetry maps. *Ocean Science*, *15*(4), 1091–1109. https://doi.org/10.5194/os-15-1091-2019

Berbery, E. H., & Nogues-Paegle, J. (1993). Intraseasonal interactions between the tropics and extratropics in the southern hemisphere. *Journal of Atmospheric Science*, *50*, 1950–1965. https://doi.org/10.1175/1520-0469(1993)050<1950:IIBTTA>2.0.CO;2

Brink, K. H. (1982). A comparison of long coastal trapped wave theory with observations off Peru. *Journal of Physical Oceanography*, *12*, 897–913.

Brink, K. H. (2018). *Stable coastal-trapped waves with stratification, topography and mean flow*. https://hdl.handle.net/1912/10527

Brunner, K., Rivas, D., & Lwiza, K. M. M. (2019). Application of classical coastal trapped wave theory to high scattering regions. *Journal of Physical Oceanography*, *49*, 2201–2216. https://doi.org/10.1175/JPO-D-18-0112.1

Clarke, A. (1992). Low-frequency reflection from a non-meridional eastern ocean boundary and the use of coastal sea level to monitor eastern Pacific equatorial Kelvin waves. *Journal of Physical Oceanography*, *22*(2), 163–183.

Clarke, A., & Ahmed, R. (1999). Dynamics of remotely forced intraseasonal oscillations off the western coast of South America. *Journal of Physical Oceanography*, *29*(2), 240–258.

Clarke, A. J., & Shi, C. (1991). Critical frequencies at ocean boundaries. *Journal of Geophysical Research*, *96*(C6), 10731–10738. https://doi.org/10.1029/91JC00933

Combes, V., & Matano, R. P. (2019). On the origins of the low-frequency sea surface height variability of the Patagonia shelf region. *Ocean Modelling*, *142*, 101454. https://doi.org/10.1016/j.ocemod.2019.101454

Conejero, C., Dewitte, B., Garçon, V., Sudre, J. & Montes, I. (2020). ENSO diversity driving low-frequency change in mesoscale activity off Peru and Chile. *Scientific Reports*, *10*, 17902.

Cravatte, S., Picaut, J., & Eldin, G. (2003). Second and first baroclinic Kelvin modes in the equatorial Pacific at intraseasonal time scales. *Journal of Geophysical Research*, *108*, 3266. https://doi.org/10.1029/2002JC001511

Dee, D. P., Uppala, S. M., Simmons, A. J., Berrisford, P., Poli, P., Kobayashi, S., et al. (2011). The ERA-interim reanalysis: Configuration and performance of the data assimilation system. *Quaterly Journal of the Royal Meteorological Society*, *137*, 553–597. https://doi.org/10.1002/qj.828

Dewitte, B., Cibot, C., Périgaud, C., An, S. I., & Terray, L. (2007). Interaction between near-annual and ENSO modes in a CGCM simulation: Role of the equatorial background mean state. *Journal of Climate*, *20*(6), 1035–1052. https://doi.org/10.1175/JCLI4060.1

Dewitte, B., Purca, S., Illig, S., Renault, L., & Giese, B. (2008). Low frequency modulation of the intraseasonal equatorial Kelvin wave activity in the Pacific Ocean from SODA: 1958-2001. *Journal of Climate*, *21*, 6060–6069.

Freitas, P. P., Paiva, A. M., Cirano, M., Mill, G. N., Costa, V. S., Gabioux, M., & França, B. R. L. (2021). Coastal trapped waves propagation along the Southwestern Atlantic Continental Shelf. *Continental Shelf Research*. https://doi.org/10.1016/j.csr.2021.104496

Hendon, H. H., Liebmann, B., & Glick, J. D. (1998). Oceanic Kelvin waves and the Madden–Julian oscillation. *Journal of Atmospheric Science*, *55*, 88–101.

Hughes, C. W., & Meredith, M. P. (2006). Coherent sea-level fluctuations along the global continental slope. *Philosophical Transactions of the Royal Society A*, *364*, 885–901. https://doi.org/10.1098/rsta.2006.1744

Huthnance, J. M. (1978). On coastal trapped waves: Analysis and numerical calculation by inverse iteration. *Journal of Physical Oceanography*, *8*, 74–92.

Illig, S., Bachelery, M.-L., & Cadier, E. (2018). Subseasonal coastal-trapped wave propagations in the southeastern Pacific and Atlantic Oceans: 2. Wave characteristics and connection with the equatorial variability. *Journal of Geophysical Research: Oceans*, *123*, 3942–3961. https://doi.org/10.1029/2017JC013540

Kessler, W., McPhaden, M., & Weickmann, K. (1995). Forcing of intra-seasonal Kelvin waves in the equatorial Pacific. *Journal of Geophysical Research*, *100*(C6), 10613–10631.

Kessler, W. S., & Kleeman, R. (2000). Rectification of the Madden–Julian oscillation into the ENSO cycle. *Journal of Climate*, *13*, 3560–3575.

Kiladis, G. N., Dias, J., Straub, K. H., Wheeler, M. C., Tulich, S. N., Kikuchi, K., et al. (2014). A comparison of OLR and circulation based indices for tracking the MJO. *Monthly Weather Review*, *142*, 1697–1715.

Lellouche, J.-M., Greiner, E., Bourdallé-Badie, R., Garric, G., Melet, A., Drévillon, M., et al. (2021). The Copernicus global 1/12° Oceanic and sea ice GLORYS12 Reanalysis. *Frontiers of Earth Science*. https://doi.org/10.3389/feart.2021.698876

Madden, R. A., & Julian, P. R. (1994). Observations of the 40–50-day tropical oscillation—A review. *Monthly Weather Review*, *122*, 814–837.

McPhaden, M. J. F. (1999). Genesis and evolution of the 1997-98 El Niño. *Science*. https://doi.org/10.1126/science.283.5404.950

Pizarro, O., Clarke, A. J., & Van Gorder, S. (2001). El Niño sea level and currents along the South American coast: Comparison of observations with theory. *Journal of Physical Oceanography*, *31*(7), 1891–1903.

Poli, L., Artana, C., Provost, C., Sirven, J., Sennéchael, N., Cuypers, Y., & Lellouche, J.-M. (2020). Anatomy of subinertial waves along the Patagonian shelf break in a 1/12 global operational model. *Journal of Geophysical Research: Oceans*. https://doi.org/10.1029/2020JC016549

Pujol, M.-I., Fauge're, Y., Taburet, G., Dupuy, S., Pelloquin, C., Ablain, M., & Picot, N. (2016). Duacs DT2014: The new multi-mission altimeter data set reprocessed over 20 years. *Ocean Science*, *12*, 1067–1090. https://doi.org/10.5194/os-12-1067-2016

Roundy, P. E., & Kiladis, G. N. (2006). Observed relationship between oceanic Kelvin waves and atmospheric forcing. *Journal of Climate*, *19*, 5253–5272. https://doi.org/10.1175/JCLI3893.1

Sprintall, J., Cravatte, S., Dewitte, B., Du, Y., & Sen Gupta, A. (2020). Oceanic teleconnections. In M. J. McPhaden, A. Santoso, & W. Cai (Eds.), *El Niño in a changing climate*. Wiley. Chapter 15.

Strub, P. T., James, C., Montecino, V., Rutllant, J. A., & Blanco, J. L. (2019). Ocean circulation along the Southern Chile transition region (38°–46°S): Mean, seasonal and interannual variability, with a focus on 2014–2016, 2019. *Progress in Oceaongraphy*, *172*, 159–198. https://doi.org/10.1016/j.pocean.2019.01.004

Vivier, F., Provost, C., & Meredith, M. (2001). Remote and local forcing in the Brazil Malvinas Region. *Journal of Physical Oceanography*, *31*, 892–913. https://doi.org/10.1175/1520-0485